coatings

MDPI

Article

Microstructure and Wear Behavior of FeCoCrNiMo0.2 High Entropy Coatings Prepared by Air Plasma Spray and the High Velocity Oxy-Fuel Spray Processes

Tianchen Li [1], Yong Liu [1], Bin Liu [1,*], Wenmin Guo [2,*] and Liyou Xu [1]

[1] State Key Laboratory for Powder Metallurgy, Central South University, Changsha 410083, China; litianchencsu@163.com (T.L.); yonliu@csu.edu.cn (Y.L.); leoxu0421@163.com (L.X.)

[2] College of Mechanical and Energy Engineering, Shaoyang University, Shaoyang 422000, China

* Correspondence: binliu@csu.edu.cn (B.L.); wenminguo@hotmail.com (W.G.); Tel.: +86-731-8887-7669 (B.L.); +86-739-530-5016 (W.G.)

Received: 31 July 2017; Accepted: 18 September 2017; Published: 20 September 2017

Abstract: In the present research, the spherical FeCoCrNiMo0.2 high entropy alloy (HEA) powders with a single FCC solid solution structure were prepared by gas atomization. Subsequently, the FeCoCrNiMo0.2 coatings with a different content of oxide inclusions were prepared by air plasma spraying (APS) and high-velocity oxy-fuel spraying (HVOF), respectively. The microstructure, phase composition, mechanical properties, and tribological behaviors of these HEA coatings were investigated. The results showed that both HEA coatings showed a typical lamellar structure with low porosity. Besides the primary FCC phase, a mixture of Fe_2O_3, Fe_3O_4, and AB_2O_4 (A = Fe, Co, Ni, and B = Fe, Cr) was identified as the oxide inclusions. The oxide content of the APS coating and HVOF coating was calculated to be 47.0% and 12.7%, respectively. The wear resistance of the APS coating was approximately one order of magnitude higher than that of the HVOF coating. It was mainly attributed to the self-lubricated effect caused by the oxide films. The mass loss of the APS coating was mainly ascribed to the breakaway of the oxide film, while the main wear mechanism of the HVOF coating was the abrasive wear.

Keywords: high entropy; thermal spray; microstructure; wear behavior

1. Introduction

In 2004, Yeh [1] first proposed a new multi-component alloy design concept named high-entropy alloys (HEAs), which broke the conventional one or two major elements alloying design strategy. These alloys contained more than four elements mixed in near equiatomic concentrations and have attracted extensive research over the past decade [1–4]. Because of the high configurational entropy, these alloys are mainly composed of disordered or ordered solid solutions, nanostructures, or even amorphous phases rather than complex brittle intermetallic compounds after solidification [5]. Compared with the conventional alloys, the most distinguished effects in HEAs are high-entropy, severe lattice distortion, sluggish diffusion, and cocktail effects. These effects might provide several important advantages including ease of getting the supersaturated state and fine precipitates, an increased recrystallization temperature, slower grain growth, a reduced particle coarsening rate, and an increased creep resistance, which might be beneficial for high mechanical properties, superior thermal stability, and excellent wear- and corrosion-resistance [3,5–8]. These outstanding properties were desirable for engineering applications, such as machinery, furnace parts, and even space [9].

Surface engineering is now a key materials technology in the design of future advanced industrial components [10–13]. Up to now, most investigations on HEAs are limited in bulk materials, and those on HEA coatings are rarely reported [14,15]. As a typical HEA, quaternary FeCoCrNi HEA with a

simple FCC solid solution was wildly investigated. Liu et al. [16] reported that the FeCoCrNi HEA is characterized by a high tensile strength of 712.5 MPa and a high elongation of 56%, indicating excellent deformation and work hardening capacity. Such good machinability makes it a reliable base for further strengthing with the addition of other principal elements. With the addition of other principal elements such as Cu, Ti, Mo, Mn, Al, Si, etc., the hardness of FeCoCrNi HEA was generally enhanced by solution hardening, precipitation strengthening, and the nanocomposite strengthening mechanism [5,17]. It was noteworthy that the FeCoCrNiMo bulk HEA was tremendously strengthened without causing a severe embrittlement [18]. Moreover, the addition of Mo provides excellent scuffing resistance to abrasive wear in coating materials [19–21]. Therefore, it could be inferred that FeCoCrNiMo HEAs would be alternative candidates for the preparation of high performance thermal spray coatings.

However, the predominant drawback to these thermal spray techniques is that their inherent high temperatures inevitably lead to changes in the coating microstructure—namely, oxide inclusions. Generally, the density, chemical composition, phase composition, and microstructure, which further resulted in hardness, bonding strength, and wear- and corrosion-resistance of thermal sprayed coatings, would be degraded by these oxide inclusions. However, some research also reported that the hardness and wear resistance of these thermal sprayed coatings could be enhanced by these oxides. Bobzin [22] found that the wear rates of the FeCrMnBC coating was significantly decreased from 1.1 $mm^3/N{\cdot}m$ to 0.01 $mm^3/N{\cdot}m$ as the increased oxide content. Similar research results were also reported by Hsu et al. [23] and Li et al. [24]. To the best of our knowledge, the microstructure evolution and the related effects on the wear behavior of the FeCoCrNi–M HEA coatings have not been reported yet.

In the present research, FeCoCrNiMo0.2 HEA coatings with different contents of oxides were prepared by air plasma spraying (APS) and high velocity oxy-fuel (HVOF) spraying, respectively. The microstructure and mechanical properties of these as-sprayed coatings were characterized. The wear behavior of the coatings was investigated and the related wear mechanisms were claimed. These research results would provide essentials for further research and applications of HEA coatings.

2. Materials and Methods

2.1. Powder Preparation

The as-cast FeCoCrNiMo0.2 HEA was prepared by vacuum arc-melting with high-purity (99.9%) Fe, Co, Cr, Ni, and Mo bulk metals. Then, the ingot was remelted and dropped through a ceramic tube, and atomized by 99.9% purity argon. The metal flow rate, atomization pressure, and gas flow rate were 50 g/s, 4 MPa, and 0.25 m^3/s, respectively. The liquid droplets dropped into the atomization chamber, cooled down, and solidified to spherical powders. The oxygen content of the powders was analyzed by nitrogen/oxgen determinator (TC600, Leco, Chicago, IL, USA). Prior to thermal spray process, the powder was sieved to obtain specified particle size distribution in the range of 15–45 μm.

2.2. Development of the Coatings

45# steel was used as the substrate in the present investigation. Before spraying, the substrate was cut into a dimension of 100 mm × 30 mm × 20 mm, subsequently polished by SiC papers down to 150-grit, ultrasonically degreased in acetone, and then grit blasted with alumina powders. The FeCoCrNiMo0.2 HEA coatings were deposited on the as-prepared substrate with the APS system (LP-60Z, BST, Jiujiang, China) and the HVOF system (JP-8000, Praxair, Danbury, CT, USA), respectively. The optimized spray parameters are shown in Table 1. The amount of layers for both HEA coatings was 12.

Table 1. Optimized spraying parameters of both high entropy alloy (HEA) coatings.

Parameters	HVOF	Parameters	APS
Powder feed rate (g/min)	40	Powder feed rate (g/min)	60
Oxygen (L/min)	370	Ar/He (L/min)	60/24
Kerosene (L/min)	0.2	Power (kW)	23
Spray distance (mm)	380	Spray distance (mm)	150
Traverse speed (mm/s)	500	Traverse speed (mm/s)	150

2.3. Coating Characterization

The microstructure of these as-sprayed coatings were characterized by scanning electron microscope (SEM, Quanta FEG250, FEI, Hillsboro, OR, USA), equipped with the energy dispersive spectrometer (EDS, X-Max, Oxford Ins., Oxford, UK). The porosity and oxide contents in the cross-section of the coatings were evaluated using image analyzer of DT2000 software (version 1.0). The element distribution was investigated with electron probe microanalysis (EPMA, EPMA-1600, JEOL, Tokyo, Japan). Phase composition was identified by X-ray diffraction (XRD, D/MAX-2250, Rigaku, Tokyo, Japan) with a Cu Kα radiation at 40 kV and 200 mA. Microhardness of the HEA coatings was measured by a Vickers microhardness tester (MicroMet5104, Buehler, Lake Bluff, IL, USA) with an indenter load of 0.2 kg. The holding time was 15 s. The nano mechanical properties were performed by using nanoindention tester (UNHT, Anton Paar, Graz, Austria). Prior to nanoindentation, the specimens were carefully polished to mirror-like appearance. Indentations were conducted in load-controlled mode at a load up to 2000 mN using loading rate of 4000 mN/min. The maximum load was held constant for 15 s and then was unloaded at the rates same as the loading one.

2.4. Tribological Trials

The tribological test of the HEA coatings was performed by using a reciprocating friction and wear tester (ZKKH, Lanzhou, China). Prior to wear testing, the specimens were ground with 1000 mesh emery papers. GCr15 balls (700 $HV_{0.2}$) were used to as the counterpart with a diameter of Φ 6 mm. The test load was 10 N and the linear speed was 50 mm/s. The wear volume was calculated by 3D profile tester (Nano Map 500Ls, Ape Tech, Saratoga, NY, USA). The volume wear rate was calculated by $W = V/F \times S$, where V is the wear volume (mm^3), F is the test load (N), and S is the sliding distance (m).

3. Results and Discussion

3.1. Characterization of the HEA Feedstock Powders

Figure 1a shows the morphology of the feedstock powders. It appeared that the powder exhibited either a spherical or near-spherical shape with some satellite structure. During the atomized process, small melts cooled faster and adhered to the surface of large droplets; therefore, typical satellite structure was formed. The cross section of the powder morphology is presented in Figure 1b. The chemical composition of the feedstock powder was evaluated by EDS, as shown in Table 2. The results were in good accord with the nominal composition as expectable. The content of oxygen of the powders was as low as 0.03 wt %, indicating that no obvious oxidation of HEA occurred during the atomizing process.

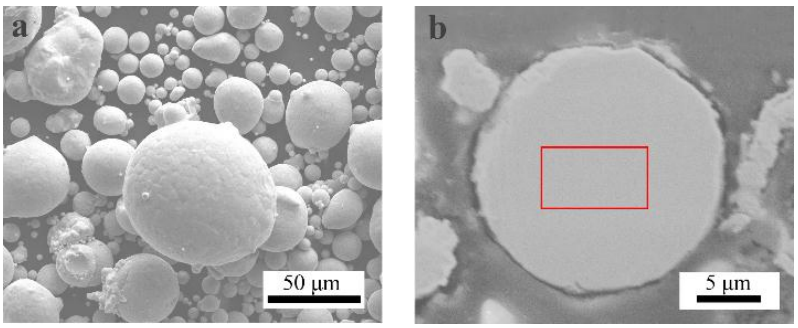

Figure 1. (**a**) Morphologies and (**b**) cross section of the gas-atomized FeCoCrNiMo0.2 HEA powders.

Table 2. Chemical compositions of gas-atomized FeCoCrNiMo0.2 HEA feedstock powder.

Elements	Actual Composition (at. %)	Nominal Composition (at. %)
Fe	23.64	23.81
Co	23.76	23.81
Cr	23.89	23.81
Ni	23.40	23.81
Mo	5.31	4.76

3.2. HEA Coatings Characterization

The XRD patterns of the feedstock powders and as-sprayed coatings were illustrated in Figure 2. It is evident that FeCoCrNiMo0.2 gas-atomized powders exhibit a single typical FCC-structure solid solution phase with diffraction peaks at 2θ = 43.66°, 50.82°, and 74.67° [18]. According to the empirical rules, solid solutions were generally formed in HEA systems under the following certain conditions. (1) The electron concentration (*VEC*) was greater than 8 [25]; (2) a new parameter combining effects of entropy and enthalpy (Ω) was proposed to be more than 1 and atomic size differences (δ) was less than 6.6% [26]. The parameters *VEC*, Ω, and δ were defined as the following equations, respectively.

$$VEC = \sum_{i=1}^{n} X_i (VEC)_i \quad (1)$$

where $(VEC)_i$ is valence electron concentration of the i_{th} component, X_i is the mole fraction of the i_{th} component.

$$\Omega = \frac{T_m \Delta S_{mix}}{|\Delta H_{mix}|} \quad (2)$$

$$\Delta S_{\text{mix}} = -\text{R} \sum_{\text{i}=1}^{\text{n}} X_{\text{i}} \ \ln X_i \quad (3)$$

where T_m is a melting temperature of the system, calculated as an average of melting temperatures of its components. R is the gas constant, 8.314 J/K·mol. ΔS_{mix} the configurational entropy.

$$\delta = \sqrt{\sum_{i=1}^{n} X_i (1 - r_i/\bar{r})^2} \quad (4)$$

where r_i is the atomic radius of i_{th} component, and $\bar{r}$ is the mean atomic radius of all elements.

In the present study, the Ω, δ, and *VEC* values for the FeCoCrNiMo0.2 HEA were calculated to be 4.237, 2, and 8.14, respectively, which tallied well with that proposed by the criterion above. Furthermore, the configurational entropy of HEA calculated by Equation (3) was 12.57. According to the Thermodynamic Second Law, the state with lowest Gibbs free energy would be the equilibrium state. As a result, such high configurational entropy is available to enhance the solid solution by means of reducing the Gibbs free energy of formation, especially at high temperature [27].

The XRD patterns of these as-sprayed coatings indicated that both of the HEA coatings were primarily composed of FCC solid solution with small amount of oxides, including a mixture of Fe_3O_4, Fe_2O_3, and some binary oxides of the chemical formula AB_2O_4 (A = Fe, Co, Ni and B = Fe, Cr). It could be concluded that no obvious phase transformation was identified except for the oxidation of feedstock powers during these thermal spray processes. Previous research proved that high entropy alloys generally exhibited high thermal stablity owing to the high entropy and sluggish diffusion effect. During the thermal spray process, each droplet cools at very high rates (>104 K/s) to form uniform, very fine-grained, polycrystalline coatings. It was apparent that FeCoCrNiMo0.2 gas-atomized powders were subjected to slight oxidation during these thermal spray processes. The results indicated that these oxides were also composed of a mixture of oxide solid solutions. On the basis of entropic effects, the random cation occupancy in spinels was known for oxide system [28,29]. According to the relative intensity of the diffraction peaks of oxides, it was concluded that the feedstock powders suffered from a much more seriously oxidation during the APS process. A broadened diffraction peaks in the XRD pattern was observed at 2θ = 43.664° in the HVOF coating, indicating a fine grain structure.

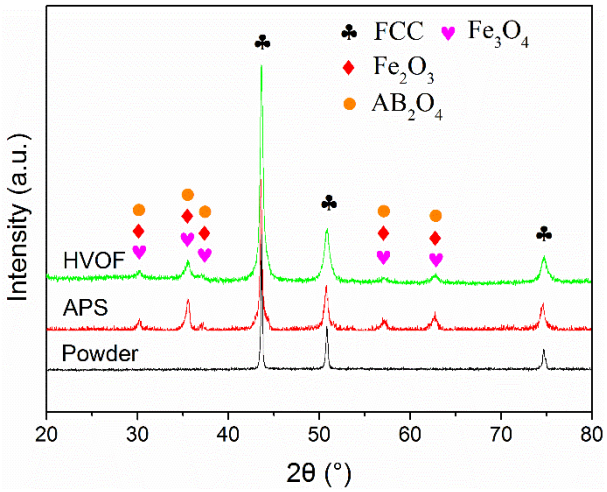

Figure 2. X-ray diffraction (XRD) pattern of the FeCoCrNiMo0.2 gas-atomized powders and the HEA coatings: oxides consist of a mixture of Fe_3O_4, Fe_2O_3, and some binary oxides with the chemical formula of AB_2O_4 (A = Fe, Co, Ni and B = Fe, Cr).

Figure 3 shows the cross-sectional SEM images of the HEA coatings prepared by APS and HVOF, respectively. It could be found that both of these coatings presented a typical lamellar structure with two obviously identifiable contrasts. The EDS analysis results (Table 3) showed that the grey region was HEA phase (labeled as A) and the dark grey region was dispersed oxide phase (labeled as B). Except for the presence of oxygen, the results indicated that no obvious changes could be detected in the chemical composition between the feedstock powders and the metal phase included in the as-sprayed coatings. The oxides content and porosity of these as-sprayed coatings was calculated and shown in Table 4. It was obvious that the APS coating has a high concentration of oxides with more microstructure defects, such as pores and inter-splat interfaces, than that in the HVOF coating. In the HVOF process, the flame temperature in the combustion chamber was reported to be up to approximately 3000 °C [30]. The feedstock powders were heated up to approximately 3000 °C and accelerated to speeds in the range of 200–1000 m/s by the combustion gas in the gun. This gives high acceleration to powder particles which were partially melted and deposited on substrate layer by layer with splat cool mechanism. In contrast, gas heating is sufficient to generate core plasma temperatures exceeding 10,000 °C during the APS process. Therefore, the feedstock powders could be melted completely and were more easily oxidized during the in-flight process than that in HVOF [30]. As the particles spread on impact, surface oxide films fractured with the flowing metal and become included

in the coatings as the oxide stringers. As shown in Figure 3c,d, pores were commonly distributed in the interface of the metal HEA phase and oxides, indicating that the formation of these microstructure defects, such as interlamellar gaps, porosity, and delamination, was significantly influenced by the oxidation behavior of the in-flight molten droplets. According to the literature [31], pores can originate by the material shrinkage on cooling from the liquid state, shadowing effect and poor wetting onto adjacent surface of the oxidized droplets.

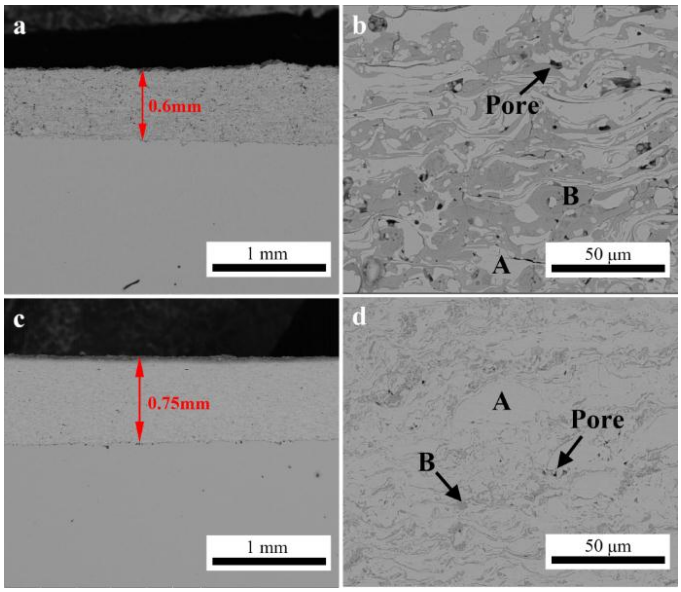

Figure 3. Cross-sectional scanning electron microscope (SEM) images of the air plasma spraying (APS) coating and the high-velocity oxy-fuel spraying (HVOF) coating at low and high magnifications. (**a**) APS coating at low magnification; (**b**) APS coating at high magnification; (**c**) HVOF coating at low magnification; (**d**) HVOF coating at high magnification.

Table 3. Composition of the as-sprayed HEA coatings determined by energy dispersive spectrometer (EDS) analysis.

Sample	Region	Fe	Co	Cr	Ni	Mo	O
APS	A	22.25	23.00	18.56	23.00	5.53	7.67
	B	15.06	11.69	17.73	10.23	3.59	41.69
HVOF	A	21.91	22.20	21.69	22.24	5.18	6.57
	B	16.94	12.41	17.55	6.10	3.77	43.23

Table 4. The oxide contents and porosity of the HEA coatings.

Sample	Oxides Content (%)	Porosity (%)
APS coating	47.0	3.1
HVOF coating	12.7	0.6

Figures 4 and 5 show the composition mapping of all the elements in the cross-sectional microstructure of these as-sprayed coatings. The results showed that the Fe, Co, Ni, Cr, and Mo elements were homogeneously distributed and enriched in the metal phase, while the O element is enriched in the grey oxide phase. It could be concluded that these coatings possessed a typical homogeneous microstructure, as reported in most of the traditional metal composite coatings.

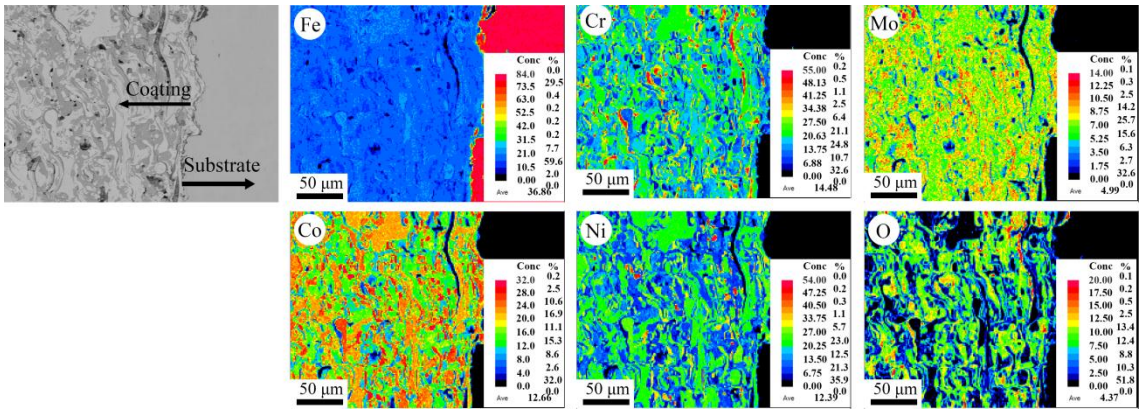

Figure 4. The elemental mapping with electron probe microanalysis (EPMA) in the APS coating.

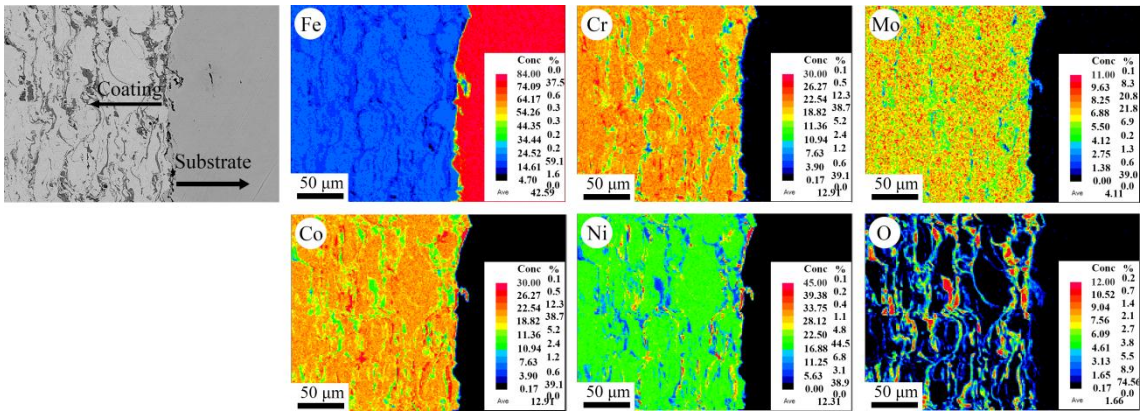

Figure 5. The elemental mapping with EPMA in the HVOF coating.

3.3. Mechanical Properties

Figure 6 presents the evolution of microhardness values of these as-sprayed coatings as a function of distance from the interface to the surface. The average microhardness values of the APS coating and HVOF coating were measured to be 356 $HV_{0.2}$ and 390 $HV_{0.2}$, respectively, which were much higher than that of the substrate and the FeCoCrNiMo0.3 bulk alloys (210 HV) [32]. Furthermore, it could be found that the microhardness values of the APS coating exhibited more drastic fluctuation than that of the HVOF coating. It was mainly ascribed to the heterogeneous microstructure with high content of oxides and defects, such as the pores and interfaces, as shown in Figure 3. Futhermore, the microhardness of the oxides in the APS coating was also characterized to be as high as 594 $HV_{0.05}$. It could be concluded that the microhardness of the APS coating was enhanced by these oxide inclusions. However, the microhardness of thermal sprayed coatings could be generally degraded by the microstructure defects, as widely reported in the literature [33,34]. In HVOF spray process, the feedstock powders was heated at a relatively low temperature and accelerated to get an ultra-high velocity [35,36]. Therefore, the HVOF coating generally possesses a homogeneous microstructure with low content of oxides and defects, resulting in the comparatively uniform microhardness measurement results.

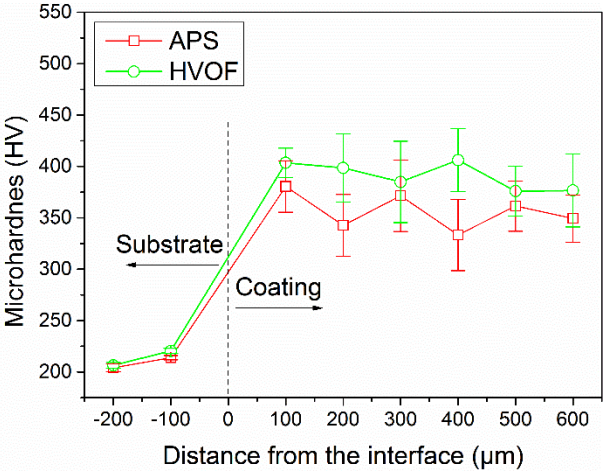

Figure 6. Microhardness profiles along the cross section of the HEA coatings.

Figure 7 plots the the load-depth curves of these thermal-sprayed coatings. The maximum indention depth h_{max} of the HEA coatings sprayed by APS and HVOF are 5.3 μm and 4.6 μm, respectively. The stiffness can be obtained by calculating the initial slope of the curve during unloading and then the value of reduced Young's modulus can be further deduced [37]. As listed in Table 5, the Young's modulus of these coatings were significantly lower than that of these bulk HEAs, such as 202 GPa for the typical FeCoCrNiMn alloy [38].

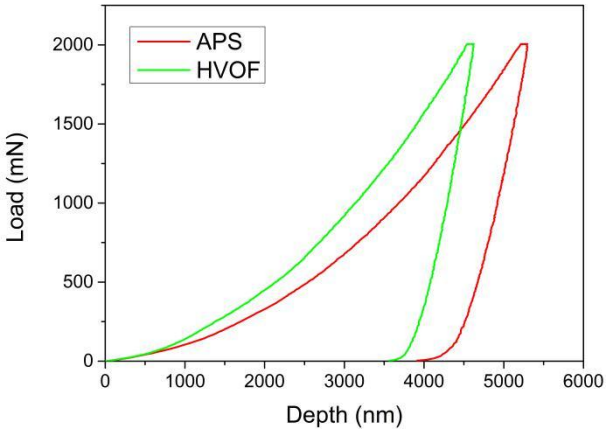

Figure 7. Load-depth curves of the HEA coatings.

Table 5. Mechanical properties of the HEA coatings.

Sample	*HIT* (GPa)	*EIT* (GPa)	*H*/*E*
APS	3.0	91.1	0.033
HVOF	4.0	127.1	0.031

3.4. Tribological Behavior

The evolution of friction coefficients of these coatings and the 45# substrate during the reciprocating wear test are displayed in Figure 8. The average friction coefficient of the HVOF coating and APS coating was approximately 0.75 and 0.84, respectively, which was much lower than 1.0 of the substrate. It can be observed that the friction coefficient curves of these coatings fluctuated up and down in the initial stage, which was mainly ascribed to the variation in the actual contact area

and adhesion between the counterpart ball. At the following stage, the friction coefficient curves tend to stabilize at a constant value. It was concluded that the contact area remains almost constant for the rest of the test. Furthermore, it was apparent that the friction curve of the HVOF coating exhibited a drastic fluctuation in the initial stage, which may be indicative of continuous formation and breaking of the transfer layer [39].

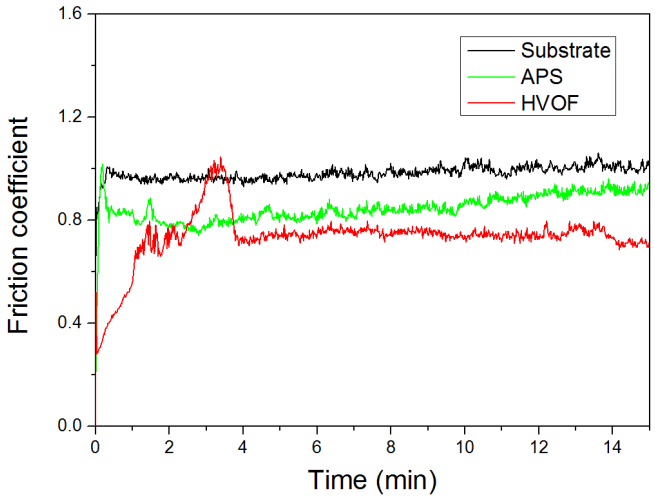

Figure 8. The friction coefficients of the APS coating, the HVOF coating, and the 45# steel substrate.

The volume wear rate was calculated to evaluate the wear resistance of these coatings, as shown in Figure 9. It was observed that the wear rate of the APS coating was approximately 3.9×10^{-5} mm^3/N·m, which was an order of magnitude lower than the 4.8×10^{-4} mm^3/N·m of HVOF coating and the 5.4×10^{-4} mm^3/N·m of the 45# steel substrate. The results indicated that the APS coating possessed the most outstanding wear resistance. Based on the results mentioned above, it could be concluded that the biggest difference between the APS and HVOF coatings was the abundant oxides inclusions and pores in the microstructure. Previous researches reported that these oxides were known as not only the reinforced particles for the enhanced microhardness, but also sometimes as the lubricant for the high wear resistance [24,40,41].

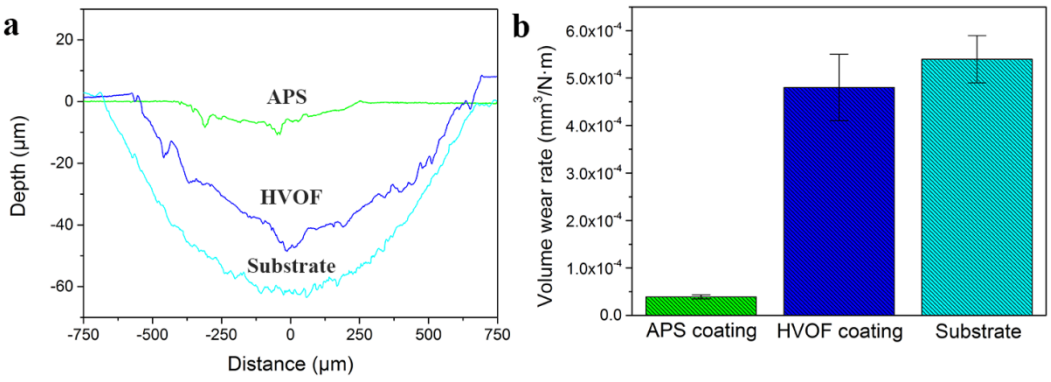

Figure 9. (**a**) The groove area measurement and (**b**) volume wear rates of the thermal-sprayed coatings.

In order to further clarify the wear mechanism, the worn surfaces of HEA coatings and 45# steel substrate are presented in Figure 10. As shown in Figure 10a,b, it was apparent that the worn surface of the 45# steel was covered by inconsecutive oxide films referred to in the relatively dark area. The EDS analysis results indicated that the oxide film was mainly composed of iron oxides, as shown in Table 6. Plenty of wear debris particles could be observed in the worn marks. The oxide scales were peeled

off along with the sliding direction of the GCr15 counterpart, indicating that the oxide scales were uncompact and exhibited a poor bonding strength with the substrate. Therefore, we can deduce that the 45# steel suffered from seriously oxidative wear.

Table 6. EDS analysis results of the worn surface of the FeCoCrNiMo0.2 coatings and the substrate.

Sample	Region	Fe	Co	Cr	Ni	Mo	O
Substrate	A	52.39	–	–	–	–	47.61
	B	100	–	–	–	–	–
APS	C	19.13	9.19	8.47	8.94	2.58	51.69
	D	21.70	21.03	19.43	22.40	4.76	10.67
	E	24.70	7.41	8.44	8.36	2.13	48.95
	F	20.64	22.81	15.19	26.91	5.45	9.00
HVOF	G	19.37	10.42	9.81	10.21	2.01	48.18
	H	21.37	21.40	21.68	21.47	4.59	9.50
	I	18.15	14.63	14.31	15.22	3.12	34.57
	J	21.14	21.16	22.56	21.03	5.00	9.11

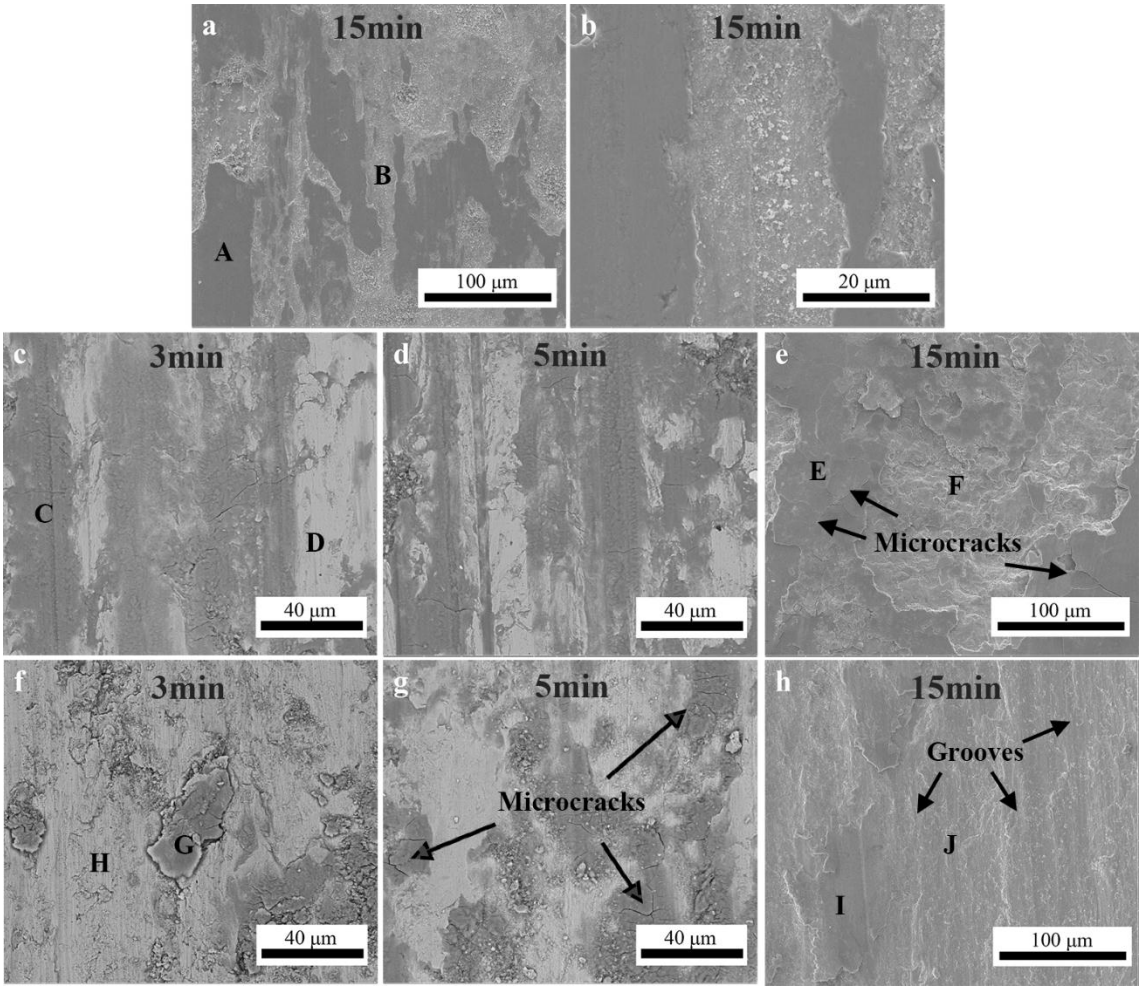

Figure 10. Worn surface morphologies of the HEA coatings and substrate after friction test under different duration: (**a**–**b**) 45# steel substrate; (**c**–**e**) the APS coating; and (**f**–**h**) the HVOF coating.

Figure 10c–e showed the worn surface morphologies of the APS coating after friction test for 3 min, 5 min, and 15 min, respectively. In the initial stage of the friction test (as shown in Figure 10c), it was obvious that small amounts of oxides was formed on the worn surface. The oxidation behavior

of the APS coating was significantly accelerated as the friction test proceeded. These oxides were trapped in the sliding surface and compacted into a layer called transfer layer, which exhibited a good adhesive strength with the APS coating. This transfer layer prevents the sliding surfaces from direct metal-to-metal contact and consequently inhibits adhesive wear [42]. As shown in Figure 10e, a thick oxide layer was formed on the worn surface of the APS coating after friction test for 15 min. This oxide layer underwent continuous stress, which can create damage. The orientation of the microcracks was disordered, revealing that the failure mechanism of the oxide scale was caused by the crack propagation. This compacted oxide layer cracked and flaked off during sliding, resulting in the formation of relatively large-sized wear debris [43].

Figure 10f–h showed the worn surface of the HVOF coating after friction test for 3 min, 5 min, and 15 min, respectively. As shown in Figure 10f,g, the worn surface of the HVOF coating also had been oxidized, caused by the frictional heating at the asperities contact. What is different from that on the APS coating is that only small portion of worn surface was covered with oxide layers. A lot of cracks could be observed within the oxide layers. The worn surface was much more uneven with a lot of large sized wear debris, which were proposed as the main reasons for the variation in the actual contact area, resulting in the drastic fluctuation of the friction coefficients in the initial stage of the friction test, as shown in Figure 8. As the friction test proceeded, ploughed grooves were clearly observed in Figure 10h. It was concluded that the dominant wear mechanism is mild abrasion and ploughing by plastic deformation.

As discussed above, both of the APS and HVOF coatings showed a superior wear resistance than that of the 45# steel substrate. It was suggested to be mainly attributed to their high hardness and the difference in wear mechanism. According to the classic wear theories, the wear resistance of materials was generally in direct proportion to its hardness or the ratio of hardness and elastic modulus [44,45]. It was apparent from Figure 9 that both of the APS and HVOF coating showed a much higher hardness than that of 45# substrate. Furthermore, the oxide scale formed on the worn surface of the 45# steel was uncompact and exhibited a poor bonding strength with the substrate.

In the present study, the average microhardness of the HEA metal phase and oxides in the APS coating, labeled as A and B in Figure 4, was measured to be 404 $HV_{0.05}$ and 594 $HV_{0.05}$, respectively. It was much higher than 332 $HV_{0.05}$ and 512 $HV_{0.05}$ of that in HVOF coating. However, the average microhardness values of the APS coating was little lower than that of the HVOF coating. It was indicated that the hardness of the APS coating could be degraded by the microstructure defects, such as the pores and the interface between the metal phase and oxide stringers. Similar research results also were reported by Guo et al. and Tian et al. [46,47]. Figure 9 indicated that the wear resistance of the APS coating was an order of magnitude higher than that of HVOF coating. It was apparent that the wear resistance properties of the APS and HVOF HEA coatings cannot be predicted according to the classic wear theories. As mentioned above, the excellent wear resistance of the APS coating can be attributed to lubricated effect caused by oxide layers [48]. However, the oxide layers formed on the worn surface of these HEA coatings could be divided into two parts. One is the oxide inclusions formed during the thermal spraying process, and the other is the oxides formed by the oxidation of the metal phase during the wear test. Previous studies reported that the FeCoNiCr–M HEA alloys exhibited excellent oxidation resistance at high temperature due to the sluggish diffusion [49,50]. Furthermore, the oxide film was suggested to have a low rate of thickening and a high resistance to spallation. However, the content of the oxide inclusions of the APS coating, which formed during the spraying process, was calculated to be as high as 47%, much higher than 12.7% of that in the HVOF coating. During sliding wear test, all the oxides could be compacted into an oxide layer by the continuous stress. Due to the abundant oxide inclusions, the transformed oxide layer on the APS coatings could be easier to be formed than that of the HVOF coating, which resulted in the superior wear resistance. Saka et al. [51] have claimed that a harder substrate is able to hold a thicker transfer oxide layer more firmly as compared to a softer one. Therefore, the oxide layer formed on the metal phase in the APS coating was suggested to be more stable than that on the HVOF coating.

4. Conclusions

1. The FeCoCrNiMo0.2 high entropy alloy coatings were successfully prepared with the APS and HVOF spray techniques. Both of the coatings showed a typical lamellar structure with low porosity. The average microhardness of the APS coating and HVOF coating was 356.4 and 390.9 $HV_{0.2}$, respectively.
2. Both the APS coating and the HVOF coating were mainly composed of a FCC solid solution phase with a small amount of oxides, which were identified as a mixture of Fe_3O_4, Fe_2O_3, and some binary oxides of the chemical formula AB_2O_4 (A = Fe, Co, Ni, and B = Fe, Cr) in a spinel structure. The results indicated that these oxides also have a large solid solubility in each other with the same phase structure due to the high entropy effect.
3. The volume wear rate of the APS coating was approximately 3.9×10^{-5} $mm^3/N{\cdot}m$, which was an order of magnitude lower than the 4.8×10^{-4} $mm^3/N{\cdot}m$ of the HVOF coating and the 5.4×10^{-4} $mm^3/N{\cdot}m$ of the substrate. The mass loss of the APS coating during the wear test was mainly attributed to the breakaway of the oxide film, which was formed on the worn surface of the APS coating. The wear mechanism of the HVOF coating is the mild abrasive wear.

Acknowledgments: This work was supported by the National Natural Science Foundation of China (51771232, 51671217), the National key research and development plan of China (2016YFB0700302), the Science and Technology Planning Project of Hunan Province of China (2015SK1002-1), the Research Foundation of Education Bureau of Hunan Province of China (17B237) and the State Key Lab of Powder Metallurgy.

Author Contributions: Yong Liu, Bin Liu, and Wenmin Guo conceived and designed the experiments Tianchen Li and Liyou Xu prepared the FeCoCrNiMo0.2 HEA coatings and performed the microstructural characterization of the coatings under the supervision of Yong Liu and Bin Liu; the mechanical testing under the supervision of Bin Liu and Wenmin Guo; and the wear test under the supervision of Yong Liu, Bin Liu and Wenmin Guo. All authors discussed the results and approved the final manuscript.

Conflicts of Interest: The authors declare no conflict of interest.

References

1. Yeh, J.-W.; Chen, S.-K.; Lin, S.-J.; Gan, J.-Y.; Chin, T.-S.; Shun, T.-T.; Tsau, C.-H.; Chang, S.-Y. Nanostructured high-entropy alloys with multiple principal elements: Novel alloy design concepts and outcomes. *Adv. Eng. Mater.* **2004**, *6*, 299–303. [CrossRef]
2. Cantor, B.; Chang, I.T.H.; Knight, P.; Vincent, A.J.B. Microstructural development in equiatomic multicomponent alloys. *Mater. Sci. Eng. A* **2004**, *375*, 213–218. [CrossRef]
3. Gludovatz, B.; Hohenwarter, A.; Catoor, D.; Chang, E.H.; George, E.P.; Ritchie, R.O. A fracture-resistant high-entropy alloy for cryogenic applications. *Science* **2014**, *345*, 1153–1158. [CrossRef] [PubMed]
4. Owen, L.R.; Pickering, E.J.; Playford, H.Y.; Stone, H.J.; Tucker, M.G.; Jones, N.G. An assessment of the lattice strain in the CrMnFeCoNi high-entropy alloy. *Acta Mater.* **2017**, *122*, 11–18. [CrossRef]
5. Miracle, D.B.; Senkov, O.N. A critical review of high entropy alloys and related concepts. *Acta Mater.* **2017**, *122*, 448–511. [CrossRef]
6. Schuh, B.; Mendez-Martin, F.; Voelker, B.; George, E.P.; Clemens, H.; Pippan, R.; Hohenwarter, A. Mechanical properties, microstructure and thermal stability of a nanocrystalline CoCrFeMnNi high-entropy alloy after severe plastic deformation. *Acta Mater.* **2015**, *96*, 258–268. [CrossRef]
7. He, Y.; Zhang, J.; Zhang, H.; Song, G. Effects of different levels of boron on microstructure and hardness of $CoCrFeNiAl_xCu_{0.7}Si_{0.1}B_y$ high-entropy alloy coatings by laser cladding. *Coatings* **2017**, *7*, 7. [CrossRef]
8. Shen, W.-J.; Tsai, M.-H.; Yeh, J.-W. Machining performance of sputter-deposited $(Al_{0.34}Cr_{0.22}Nb_{0.11}Si_{0.11}Ti_{0.22})_{50}N_{50}$ high-entropy nitride coatings. *Coatings* **2015**, *5*, 312–325. [CrossRef]
9. Mishra, A.K.; Samal, S.; Biswas, K. Solidification behaviour of Ti–Cu–Fe–Co–Ni high entropy alloys. *Trans. Indian Inst. Met.* **2012**, *65*, 725–730. [CrossRef]
10. Yue, T.; Xie, H.; Lin, X.; Yang, H.; Meng, G. Microstructure of laser re-melted AlCoCrCuFeNi high entropy alloy coatings produced by plasma spraying. *Entropy* **2013**, *15*, 2833–2845. [CrossRef]
11. Yu, Z.; Ma, H.; Spolenak, R. Ultrastrong ductile and stable high-entropy alloys at small scales. *Nat. Commun.* **2015**, *6*, 7748. [CrossRef]

12. Wang, X.-R.; Wang, Z.-Q.; Lin, T.-S.; He, P. Mass transfer trends of AlCoCrFeNi high-entropy alloy coatings on TC11 substrate via electrospark—Computer numerical control deposition. *J. Mater. Process. Technol.* **2017**, *241*, 93–102. [CrossRef]
13. Shang, C.; Axinte, E.; Sun, J.; Li, X.; Li, P.; Du, J.; Qiao, P.; Wang, Y. CoCrFeNi($W_{1-x}Mo_x$) high-entropy alloy coatings with excellent mechanical properties and corrosion resistance prepared by mechanical alloying and hot pressing sintering. *Mater. Des.* **2017**, *117*, 193–202. [CrossRef]
14. Li, Z.; Pradeep, K.G.; Deng, Y.; Raabe, D.; Tasan, C.C. Metastable high-entropy dual-phase alloys overcome the strength-ductility trade-off. *Nature* **2016**, *534*, 227–230. [CrossRef] [PubMed]
15. Zhang, Z.J.; Mao, M.M.; Wang, J.; Bernd, G.; Zhang, Z.; Mao, S.X.; George, E.P.; Qian, Y.; Ritchie, R.O. Nanoscale origins of the damage tolerance of the high-entropy alloy crmnfeconi. *Nat. Commun.* **2015**, *6*, 10143. [CrossRef] [PubMed]
16. Liu, B.; Wang, J.; Liu, Y.; Fang, Q.; Wu, Y.; Chen, S.; Liu, C.T. Microstructure and mechanical properties of equimolar FeCoCrNi high entropy alloy prepared via powder extrusion. *Intermetallics* **2016**, *75*, 25–30. [CrossRef]
17. He, J.; Wang, H.; Wu, Y.; Liu, X.; Mao, H.; Nieh, T.G.; Lu, Z. Precipitation behavior and its effects on tensile properties of FeCoNiCr high-entropy alloys. *Intermetallics* **2016**, *79*, 41–52. [CrossRef]
18. Liu, W.H.; Lu, Z.P.; He, J.Y.; Luan, J.H.; Wang, Z.J.; Liu, B.; Liu, Y.; Chen, M.W.; Liu, C.T. Ductile CoCrFeNiMo*x* high entropy alloys strengthened by hard intermetallic phases. *Acta Mater.* **2016**, *116*, 332–342. [CrossRef]
19. Liu, Z.Q.; Hua, M. Wear transitions and mechanisms in lubricated sliding of a molybdenum coating. *Tribol. Int.* **1999**, *32*, 499–506. [CrossRef]
20. Wayne, S.F.; Sampath, S.; Anand, V. Wear mechanisms in thermally-sprayed Mo-based coatings. *Tribol. Trans.* **1994**, *37*, 636–640. [CrossRef]
21. Lee, I.; Park, H.; Kim, J.; Lee, C. Correlation of microstructure with tribological properties in atmospheric plasma sprayed Mo-added ferrous coating. *Surf. Coat. Technol.* **2016**, *307*, 908–914. [CrossRef]
22. Bobzin, K.; Zhao, L.; Oete, M.; Koenigstein, T. Novel Fe-based wear and corrosion resistant coatings by three-cathode plasma technology. *Surf. Coat. Technol.* **2017**, *318*, 288–292. [CrossRef]
23. Hsu, W.L.; Murakami, H.; Yeh, J.W.; Yeh, A.C.; Shimoda, K. On the study of thermal-sprayed $Ni_{0.2}Co_{0.6}Fe_{0.2}CrSi_{0.2}AlTi_{0.2}$ HEA overlay coating. *Surf. Coat. Technol.* **2017**, *316*, 71–74. [CrossRef]
24. Li, B.; Gao, Y.; Han, M.; Guo, H.; Jia, J.; Wang, W.; Deng, H. Tribological properties of NiAl matrix composite coatings synthesized by plasma spraying method. *J. Mater. Res.* **2017**, *32*, 1674–1681. [CrossRef]
25. Guo, S.; Ng, C.; Lu, J.; Liu, C.T. Effect of valence electron concentration on stability of fcc or bcc phase in high entropy alloys. *J. Appl. Phys.* **2011**, *109*, 103505. [CrossRef]
26. Zhang, Y.; Zhou, Y.J.; Lin, J.P.; Chen, G.L.; Liaw, P.K. Solid-solution phase formation rules for multi-component alloys. *Adv. Eng. Mater.* **2010**, *10*, 534–538. [CrossRef]
27. Yeh, J.W. Alloy design strategies and future trends in high-entropy alloys. *JOM* **2013**, *65*, 1759–1771. [CrossRef]
28. Navrotsky, A.; Kleppa, O.J. The thermodynamics of cation distributions in simple spinels. *J. Inorg. Nucl. Chem.* **1967**, *29*, 2701–2714. [CrossRef]
29. Rost, C.M.; Sachet, E.; Borman, T.; Moballegh, A.; Dickey, E.C.; Hou, D.; Jones, J.L.; Curtarolo, S.; Maria, J.P. Entropy-stabilized oxides. *Nat. Commun.* **2015**, *6*, 8485. [CrossRef] [PubMed]
30. Mori, T.; Kuroda, S.; Murakami, H.; Katanoda, H.; Sakamoto, Y.; Newman, S. Effects of initial oxidation on β phase depletion and oxidation of conicraly bond coatings fabricated by warm spray and HVOF processes. *Surf. Coat. Technol.* **2013**, *221*, 59–69. [CrossRef]
31. Davis, J.R. *Handbook of Thermal Spray Technology*; ASM International: Materials Park, OH, USA, 2005.
32. Shun, T.-T.; Chang, L.-Y.; Shiu, M.-H. Microstructure and mechanical properties of multiprincipal component cocrfenimox alloys. *Mater. Charact.* **2012**, *70*, 63–67. [CrossRef]
33. Karaoglanli, A.C.; Oge, M.; Doleker, K.M.; Hotamis, M. Comparison of tribological properties of HVOF sprayed coatings with different composition. *Surf. Coat. Technol.* **2017**, *318*, 299–308. [CrossRef]
34. Zhao, X.B.; Ye, Z.H. Microstructure and wear resistance of molybdenum based amorphous nanocrystalline alloy coating fabricated by atmospheric plasma spraying. *Surf. Coat. Technol.* **2013**, *228*, S266–S270. [CrossRef]
35. Kuroda, S.; Jin, K.; Watanabe, M.; Katanoda, H. Warm spraying—A novel coating process based on high-velocity impact of solid particles. *Sci. Technol. Adv. Mater.* **2008**, *9*, 033002. [CrossRef] [PubMed]

36. Zhao, L.; Maurer, M.; Fischer, F.; Dicks, R.; Lugscheider, E. Influence of spray parameters on the particle in-flight properties and the properties of HVOF coating of WC–CoCr. *Wear* **2004**, *257*, 41–46. [CrossRef]
37. Pharr, G.M. Measurement of mechanical properties by ultra-low load indentation. *Mater. Sci. Eng. A* **1998**, *253*, 151–159. [CrossRef]
38. Zhu, C.; Lu, Z.; Nieh, T.G. Incipient plasticity and dislocation nucleation of FeCoCrNiMn high-entropy alloy. *Acta Mater.* **2013**, *61*, 2993–3001. [CrossRef]
39. Singh, H.; Sidhu, B.S.; Prakash, S. Performance of HVOF sprayed NiCr and Stellite-6 coatings under pin on disc wear testing. *Mater. Sci. Forum* **2011**, *701*, 21–29.
40. Tao, C.; Wang, L.; Song, X. High-temperature frictional wear behavior of MCrAlY-based coatings deposited by atmosphere plasma spraying. *Int. J. Miner. Metall. Mater.* **2017**, *24*, 222–228. [CrossRef]
41. Tyagi, R.; Xiong, D.S.; Li, J.; Dai, J. Elevated temperature tribological behavior of Ni-based composites containing nano-silver and hBN. *Wear* **2010**, *269*, 884–890. [CrossRef]
42. Lee, K.-Y.; Lee, S.-H.; Kim, Y.; Hong, H.; Oh, Y.-M.; Kim, S.-J. The effects of additive elements on the sliding wear behavior of Fe-base hardfacing alloys. *Wear* **2003**, *255*, 481–488. [CrossRef]
43. Tyagi, R.; Nath, S.K.; Ray, S. Dry sliding friction and wear in plain carbon dual phase steel. *Metall. Mater. Trans. A* **2001**, *32*, 359–367. [CrossRef]
44. Leyland, A.; Matthews, A. On the significance of the *H/E* ratio in wear control: A nanocomposite coating approach to optimised tribological behaviour. *Wear* **2000**, *246*, 1–11. [CrossRef]
45. Archard, J.F. Contact and rubbing of flat surfaces. *J. Appl. Phys.* **1953**, *24*, 981–988. [CrossRef]
46. Guo, W.; Wu, Y.; Zhang, J.; Hong, S.; Li, G.; Ying, G.; Guo, J.; Qin, Y. Fabrication and characterization of thermal-sprayed Fe-based amorphous/nanocrystalline composite coatings: An overview. *J. Therm. Spray Technol.* **2014**, *23*, 1157–1180. [CrossRef]
47. Tian, L.-H.; Xiong, W.; Liu, C.; Lu, S.; Fu, M. Microstructure and wear behavior of atmospheric plasma-sprayed AlCoCrFeNiTi high-entropy alloy coating. *J. Mater. Eng. Perform.* **2016**, *25*, 5513–5521. [CrossRef]
48. Quinn, T.F.J. Review of oxidational wear: Part I: The origins of oxidational wear. *Tribol. Int.* **1983**, *16*, 257–271. [CrossRef]
49. Gorr, B.; Mueller, F.; Christ, H.J.; Mueller, T.; Chen, H.; Kauffmann, A.; Heilmaier, M. High temperature oxidation behavior of an equimolar refractory metal-based alloy 20Nb–20Mo–20Cr–20Ti–20Al with and without Si addition. *J. Alloys Compd.* **2016**, *688*, 468–477. [CrossRef]
50. Kai, W.; Cheng, F.P.; Liao, C.Y.; Li, C.C.; Huang, R.T.; Kai, J.J. The oxidation behavior of the quinary $FeCoNiCrSi_x$ high-entropy alloys. *Mater. Chem. Phys.* **2017**, 1–8. [CrossRef]
51. Saka, N.; Pamies-Teixeira, J.J.; Suh, N.P. Wear of two-phase metals. *Wear* **1977**, *44*, 77–86. [CrossRef]